



X-Ray Emission from the Nuclear Region of Arp 220

Alessandro Paggi¹, Giuseppina Fabbiano¹, Guido Risaliti^{1,2}, Junfeng Wang³, Margarita Karovska¹, Martin Elvis¹,
W. Peter Maksym¹, Jonathan McDowell¹, and Jay Gallagher⁴

¹ Harvard-Smithsonian Center for Astrophysics, 60 Garden Street, Cambridge, MA 02138, USA; apaggi@cfa.harvard.edu

² INAF-Arcetri Observatory, Largo E. Fermi 5, I-50125 Firenze, Italy

³ Department of Astronomy and Institute of Theoretical Physics and Astrophysics, Xiamen University, Xiamen, 361005, China

⁴ Department of Astronomy, University of Wisconsin, Madison, WI 53706-1582, USA

Received 2017 March 7; revised 2017 April 30; accepted 2017 May 3; published 2017 May 23

Abstract

We present an imaging and spectral analysis of the nuclear region of the ultraluminous infrared galaxy merger of Arp 220, using deep *Chandra*-ACIS observations summing up to ~ 300 ks. Narrowband imaging with subpixel resolution of the innermost nuclear region reveals two distinct Fe–K emitting sources, coincident with the infrared and radio nuclear clusters. These sources are separated by $1'$ (~ 380 pc). The X-ray emission is extended and elongated in the eastern (E) nucleus, like the disk emission observed in millimeter radio images, suggesting a starburst dominance in this region. We estimate an Fe–K equivalent width of $\gtrsim 1$ keV for both sources and observe 2–10 keV luminosities of $\sim 2 \times 10^{40}$ erg s^{−1} (western, W) and $\sim 3 \times 10^{40}$ erg s^{−1} (E). In the 6–7 keV band the emission from these regions is dominated by the 6.7 keV Fe xxv line, suggesting a contribution from collisionally ionized gas. The thermal energy content of this gas is consistent with the kinetic energy injection in the interstellar medium by SNe II. However, nuclear winds from a hidden active galactic nucleus (AGN) ($v \sim 2000$ km s^{−1}) cannot be excluded. The 3σ upper limits on the neutral Fe–K α flux of the nuclear regions correspond to the intrinsic AGN 2–10 keV luminosities of $< 1 \times 10^{42}$ erg s^{−1} (W) and $< 0.4 \times 10^{42}$ erg s^{−1} (E). For typical AGN spectral energy distributions the bolometric luminosities are $< 3 \times 10^{43}$ erg s^{−1} (W) and $< 8 \times 10^{43}$ erg s^{−1} (E), and black hole masses of $< 1 \times 10^5 M_{\odot}$ (W) and $< 5 \times 10^5 M_{\odot}$ (E) are evaluated for Eddington limited AGNs with a standard 10% efficiency.

Key words: galaxies: active – galaxies: individual (Arp 220) – galaxies: interactions – X-rays: galaxies

1. Introduction

At a distance of 80 Mpc (Kim & Sanders 1998), Arp 220 (IC 4553/4) is both a merger and the nearest ultraluminous infrared (IR) galaxy (ULIRG; Soifer et al. 1987; Sanders & Mirabel 1996). Near-IR high-resolution ($0''.1$) NICMOS-*Hubble Space Telescope* imaging identifies the two nuclear regions of the merging galaxies, which are coincident with the two components of a double radio source (Baan & Haschick 1995; Scoville et al. 1998). At a separation of $1''$ (380 pc at a distance of 80 Mpc⁵), these nuclei are closer together than the nuclei of NGC 6240 (~ 690 pc separation; Komossa et al. 2003) and may therefore be subject to even stronger gravitational interaction, leading to accretion on the nuclei of the merging galaxies (e.g., Governato et al. 1994; Mayer et al. 2007).

The presence of an active galactic nucleus (AGN) emission in addition to intense star formation in the two nuclei has been debated. It is also not clear where this AGN emission may reside. AGN contribution to the bolometric luminosity between $\sim 5\%$ and $\sim 25\%$ ($0.1\text{--}0.4 \times 10^{12} L_{\odot}$) is suggested by the Spitzer mid-IR spectrum of the central $8''$ region of Arp 220 (Veilleux et al. 2009; Nardini et al. 2010); more recent *Herschel* results (Rangwala et al. 2011) and modeling of the nuclear spectra (Contini 2013) agree with this conclusion. In the western (W) nucleus of Arp 220 the presence of a maser (Aalto et al. 2009) and a rotating massive molecular disk (Downes & Eckart 2007) suggests a massive nuclear black hole. Instead, IRAM-Plateau de Bure Interferometer (PdBI) observations (König et al. 2012) showed an extended structure in the

mm-CO gas emission in the eastern (E) nucleus of Arp 220, elongated in the northeast–southwest (NE–SW) direction, and suggested a highly dust-obscured nucleus lying between the two near-IR sources detected by Scoville et al. (1998). Recently, an analysis of 3.5 and 1.2 mm IRAM-PdBI data performed by Tunnard et al. (2015) provided evidence of significant chemical differences between the two nuclei. These authors argued for a significant AGN contribution to the W nucleus luminosity and starburst dominance in the E nucleus. ALMA imaging at 350 and 696 GHz (Scoville et al. 2015) suggested compact nuclear disks with masses of ~ 4 and $\sim 2 \times 10^9 M_{\odot}$ for the W and the E nuclei, respectively, within a radius of ~ 70 pc. High-resolution very large array (VLA) observations at 33 and 6 GHz by Barcos-Muñoz et al. (2015) showed double radio morphology. These authors estimated high hydrogen column densities $\sim 10^{25}$ cm^{−2} and star formation rate (SFR) surface densities that are among the most extreme measured for any star-forming system ($\sim 10^4 M_{\odot}$ yr^{−1} kpc^{−2}) for both nuclei, without any compelling evidence of an AGN dominating the nuclei emission at 33 GHz.

The M- σ relation (e.g., Magorrian et al. 1998) has suggested that the evolution of galaxies and supermassive nuclear black holes (SMBHs) are linked. Both the stellar population and the SMBH of a galaxy are thought to grow and evolve by the merging of smaller gas-rich galaxies and their nuclear SMBHs (Di Matteo et al. 2005; Hopkins et al. 2008). During this process, the SMBH may be “buried” by thick molecular gas, which feeds the SMBH at high rates, causing the birth of an obscured Compton Thick (CT; Risaliti et al. 1999; Levenson et al. 2006) AGN. In this paper we reexamine the X-ray emission of Arp 220. A high-resolution study of the archival

⁵ In the following analysis, we adopt the standard flat cosmology with $\Omega_{\Lambda} = 0.69$ and $H_0 = 68$ km s^{−1} Mpc^{−1} (Planck Collaboration et al. 2016).

Table 1
Summary of *Chandra* Observations of Arp 220

OBSID	Date	Exposure (ks)	PI	0.5–8 keV Counts (central 5" region)
00869	2000 Jun 24	57	Clements	583
16092	2014 Apr 30	170	Fabbiano	1390
16093	2014 Jun 24	67	Fabbiano	543

~57 ks *Chandra*-ACIS observation (OBSID 869; Clements et al. 2002) measured the hard X-ray luminosity of the central AGN but had an insufficient signal-to-noise ratio and spatial resolution to detect a line or to spatially untangle the complex central emission. The X-ray spectrum extracted from the central ~3" region suggested a hard continuum and a ~6.6 keV Fe–K emission line. A subsequent *XMM-Newton* observation detected an Fe–K line emission centered at 6.7 keV with an equivalent width (EW) of ~1.9 keV (Iwasawa et al. 2005), suggesting a highly photoionized, low-density gas illuminated by a hidden CT AGN. A reanalysis of the *Chandra* and *XMM-Newton* data (LaMassa et al. 2011) only managed to set an upper limit on the neutral Fe–K α emission at 6.4 keV.

Here we make use of new deep *Chandra*-ACIS data. Together with the archival observation, we reach a total exposure of ~300 ks, which allows us to perform a study of the X-ray emission from the nuclear region of Arp 220 with unprecedented detail by means of subpixel imaging of *Chandra*-ACIS data in narrow spectral ranges. This technique has been used successfully to study crowded emission regions of nearby Seyferts (e.g., in NGC 4151; Wang et al. 2011a, 2011b, 2011c; in Mrk 573; Paggi et al. 2012). Our new look at the nuclear region of Arp 220 has resulted in the discovery of two sources in the 6–7 keV Fe–K band, spatially coincident with the near-IR and radio positions. In Section 2 we present the data reduction procedures for the imaging and spectral analysis; in Section 3 we discuss and interpret our results; in Section 4 we draw our conclusions. In the following analysis we fix the galactic absorption to the value $N_{\text{H,gal}} = 3.9 \times 10^{20} \text{ cm}^{-2}$.

2. Data Reduction

Chandra observations used in this analysis are listed in Table 1. Level 2 event files were retrieved from the *Chandra* Data Archive⁶ and reduced with the CIAO (Fruscione et al. 2006) 4.7 software and the *Chandra* Calibration Data Base (CALDB) 4.6.7, adopting standard procedures. After excluding time intervals of background flares exceeding 3σ with the LC_SIGMA_CLIP task, we obtained a low-background total exposure time of ~290 ks. The nucleus has no significant pileup, as measured by the CIAO PILEUP_MAP tool.⁷

2.1. Imaging Analysis

Imaging analysis was performed without pixel randomization to take advantage of the telescope dithering in event positioning and with the subpixel event repositioning (SER) procedure (Li et al. 2003). We used a pixel size that was 1/4 of 0".492, the native *Chandra*-ACIS detector pixel (see, e.g., Harris et al. 2004;

Siemiginowska et al. 2007; Perlman et al. 2010; Wang et al. 2011c). Using the same Orion ACIS-S data as in the calibration of Li et al. (2003), we find a significant $\Delta = 50\%$ improvement in the point-spread function (PSF) FWHM as defined in Li et al. 2003 from subpixel repositioning for an on-axis source at 6–7 keV ($\Delta = 70\%$ at ~2 keV because of the narrower PSF at larger energies). Most of the imaging improvement is from the SER procedure (Li et al. 2003) without pixel randomization to take advantage of the sampling of the PSF by the well-characterized spacecraft dither motion. Because of the similarly “peaked” inner PSF, this is similarly effective at 2 and at 6 keV.

In the top panels of Figure 1 we show the central 5" region of Arp 220 as imaged by the three *Chandra*-ACIS observations in the broad 0.5–8 keV band with a native 0".492 pixel size. To merge the three exposures we first used the WAVDETECT task to identify point sources in the field of each observation (excluding the central region). We then used the REPROJECT_ASPECT task to modify the aspect solutions, minimizing the position differences between these sources, and finally merged the realigned images with the REPROJECT_EVENTS task to reproject the event files to the deepest 16092 observation. The relative shift between the observations is ~0".5, comparable with the 0".6 *Chandra* astrometric uncertainty.

In the bottom panels of Figure 1 the same central 5" region is shown in the narrow Fe–K 6–7 keV band with a subpixel binning of 1/4 of the native pixel size and 3×3 pixel FWHM Gaussian filter smoothing. The narrowband images for the deeper observations—16092 and 16093—show two sources associated with the W and E Arp 220 nuclei separated by 1" (~380 pc at the source distance), while in the shorter 00869 observation only the W nucleus is detected. The locations of these unique emission regions strongly argue for an identification of these sources with the nuclei of the merging galaxies. On the same panels we also show in green the position of the *Chandra* PSF artifacts as obtained with the MAKE_PSF_ASYMMETRY_REGION⁸ tool for the two nuclei. PSF asymmetries are expected in the north–west (N–W) direction for Obs ID 869 and in the N–E direction for Obs IDs 16092 and 16093 (due to different roll angles). The two nuclear sources are not affected by PSF asymmetries, but the extension in the N–E direction of the E source, shown in the deepest observation (16092), overlaps with the region of the *Chandra* PSF asymmetry—however, this can account for only up to 10% of the counts of this feature. The resulting merged images are shown in Figure 2 in the 3–6 (left panel) and 6.4–6.7 (central panel) keV bands with a subpixel binning that is 1/4 of the native pixel size. In addition, in the right panel of the same figure we show the 6.4–6.7 keV band image after continuum (3–6 keV) subtraction (see Section 2.2). These images are indicative of the continuum and Fe XXV line emission. The regions of the W and E nuclei considered for spectral extraction discussed in Section 2.2 are shown as white circles.

Using PSF simulations performed with the *Chandra* Ray Tracer⁹ (Carter et al. 2003) and taking into account the source spectrum, exposure time, and off-axis angle, we applied the Expectation through Markov Chain Monte Carlo (Esch et al. 2004; Karovska et al. 2005, 2007; Wang et al. 2014) PSF-deconvolution algorithm to the merged images of the narrowband emission. This

⁶ <http://cda.harvard.edu/chaser>

⁷ Pileup occurs on X-ray CCDs for sources with high flux levels when two or more photons arrive within the same detector region within a single CCD frame integration time, and they are counted as a single photon of higher energy (Davis 2001).

⁸ http://cxc.harvard.edu/ciao/ahelp/make_psf_asymmetry_region.html

⁹ <http://cxc.harvard.edu/chart/>

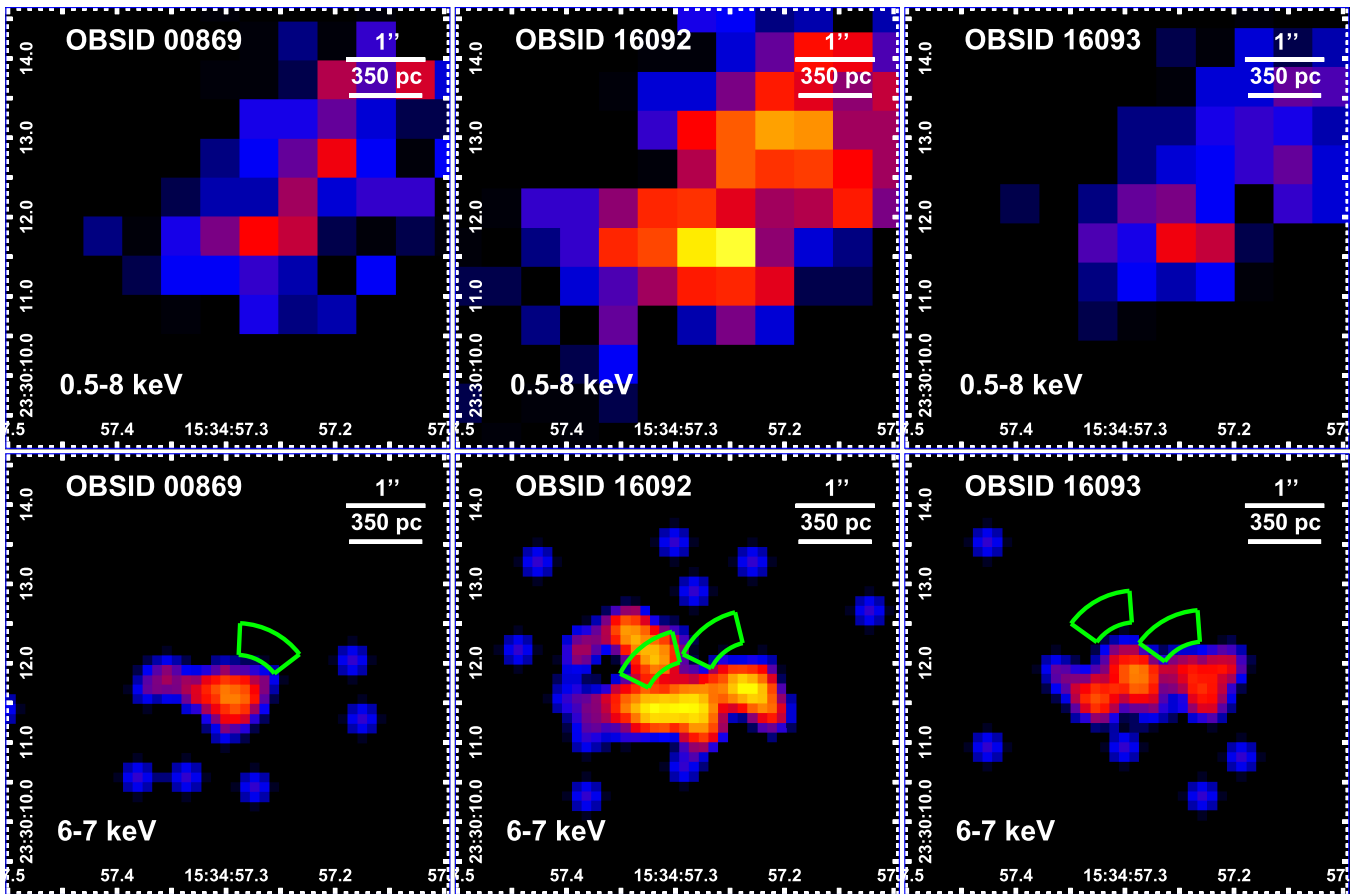


Figure 1. Top panels: broadband 0.5–8 keV images of the central $\sim 5''$ region of Arp 220 for three *Chandra*-ACIS observations reprojected on OBSID 16092, with a native $0''.492$ pixel size. Bottom panels: same as top panels but in narrowband 6–7 keV. Images are presented with a subpixel binning (1/4 of the native pixel size) and 3×3 pixel FWHM Gaussian filter smoothing. Green regions show the location of the *Chandra* PSF artifacts for the two nuclei.

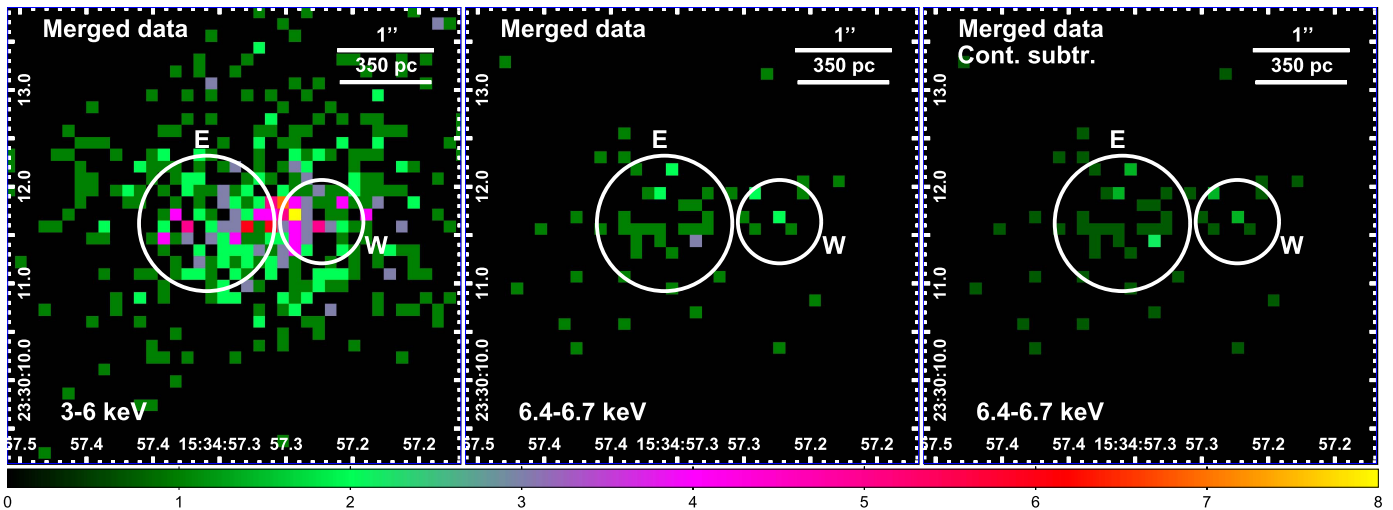


Figure 2. From left to right: merged *Chandra*-ACIS 3–6 and 6.4–6.7 keV images, indicative of continuum and Fe XXV line emission, respectively. In the right panel we show the 6.4–6.7 keV band image after continuum (3–6 keV) subtraction. Images are presented with a subpixel binning that is 1/4 of the native pixel size. The regions of spectral extraction considered in Section 2.2 are shown as white circles.

method yields a multiscale image reconstruction specifically applicable to Poisson noise-limited data.

As noted by Clements et al. (2002), the lack of U.S. Naval Observatory–detected stars in the Arp 220 field does not allow

accurate absolute astrometry using field stars. However, a comparison between the merged 6–7 keV *Chandra*-ACIS image and the high-resolution 33 GHz VLA observations (Barcos-Muñoz et al. 2015) shows a clear similarity in the morphology of

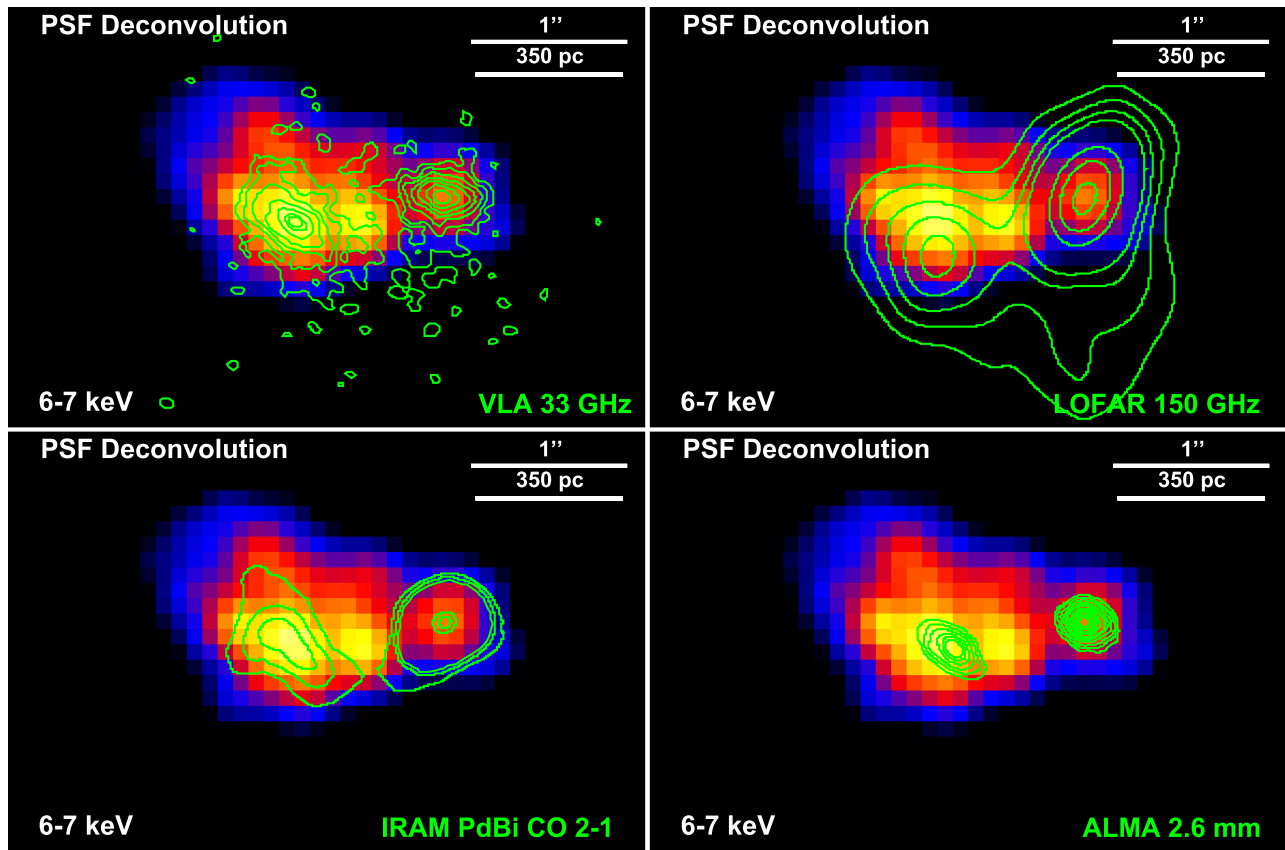


Figure 3. A merged, PSF-deconvolved *Chandra*-ACIS 6–7 keV image with a subpixel binning that is 1/5 of the native pixel size and 3×3 pixel FWHM Gaussian filter smoothing, with superimposed (from top left to bottom right) contours from the 33 GHz VLA data (Barcos-Muñoz et al. 2015), the 150 MHz continuum and the CO 2-1 IRAM PdBI data (Varenius et al. 2016), and the 2.6 mm continuum ALMA data (Scoville et al. 2017), registered as discussed in the main text.

the nuclei. In order to highlight the morphological similarity between the X-ray and the radio emission, we shifted the VLA 33 GHz sources, moving the latter in the NE direction by $\sim 0''.2$ (compatible with the *Chandra* astrometric accuracy; Rots & Budavári 2011) in order to match the position of the W radio lobe with the W X-ray nucleus, which appears less extended and therefore allows more accurate positioning. The result of this registration procedure is shown in Figure 3. In both the X-ray image and the radio contours the W nucleus looks compact while the E nucleus appears somewhat extended. We performed a similar registration with radio contours of an 150 MHz LOFAR continuum and CO 2-1 IRAM PdBI images (Varenius et al. 2016) and with 2.6 mm continuum ALMA images (Scoville et al. 2017). Again we matched the W nuclei. We notice that the positions of the W lobes in VLA 33 GHz, LOFAR 150 MHz, IRAM PdBI CO 2-1, and ALMA 2.6 mm images differ less, by $\sim 0''.1$, and therefore the use of these maps yields similar results. In all cases the deconvolved X-ray image shows a more compact emission from the W nucleus and a more extended E nucleus with a morphology similar to that of the 33 GHz, CO 2-1, and 2.6 mm radio emissions, suggesting starburst dominance in this region. On the other hand, the E X-ray nucleus lies somewhat north of the E lobe observed in the 150 MHz continuum LOFAR image. The central peak corresponds with the X4 X-ray source from Clements et al. (2002). Since the registration of radio images to the X-ray data yields similar results, in the following analysis we compare this to the VLA 33 GHz data.

Figure 4 compares the *Chandra* merged images in the 3–6 keV continuum with the observed 6–7 keV band selected to represent both the 6.4 keV emitted Fe K- α neutral line and the 6.7 keV Fe XXV line. The 3–6 keV continuum emission centroid lies between the peaks of the nuclear line emission (although it is closer to the W nucleus). The 6–7 keV peak coincides with the near-IR sources reported by Clements et al. (2002), and the 5 GHz peaks. The Fe 6–7 keV image suggests a more extended E nucleus emission with respect to the W nucleus emission. The X1 source reported by Clements et al. (2002) in the first 57 ks *Chandra* data set coincides with the W nucleus, while the X4 source from the same study lies between the two nuclei and is coincident with the central peak seen in the PSF-deconvolved 6–7 keV image.

2.2. Spectral Analysis

We attempted a spectral characterization of the emission, extracting 3–8 keV spectra from the two circular regions indicated in Figure 2. The two easternmost peaks shown in Figure 3 do not have enough counts to be studied separately (see Table 2) and we therefore selected a region that encompasses them both. Spectra were extracted with THE CIAO SPEXTRACT task, applying a point-source aperture correction, binned to obtain a minimum of five counts per bin, and fitted employing the Cash statistic.

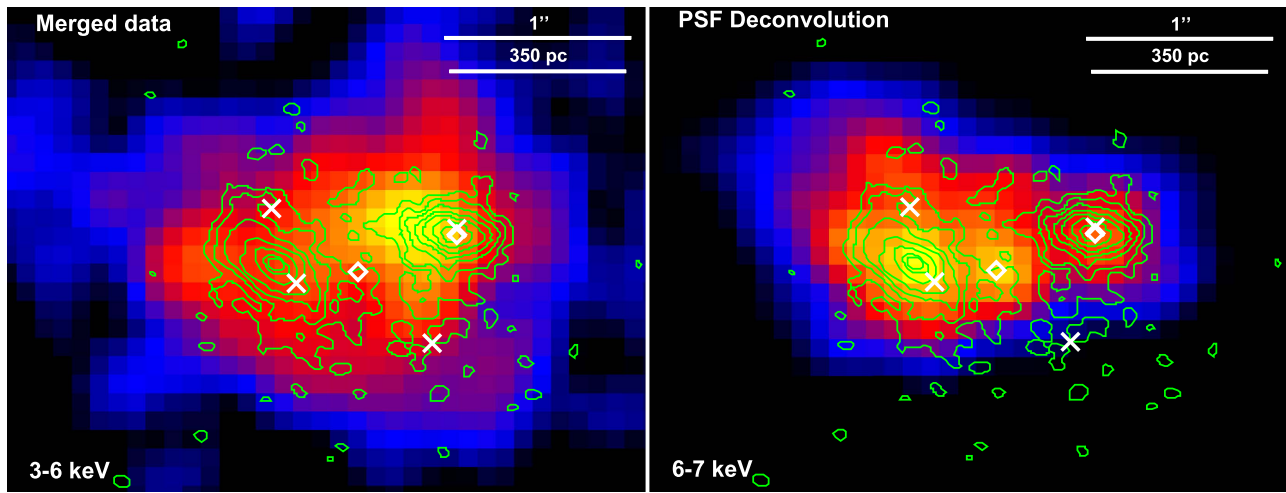


Figure 4. Merged *Chandra*-ACIS 3–6 keV (left panel) and 6–7 keV PSF-deconvolved (right panel) images, indicative of continuum and Fe line emission, respectively. Images are presented with a subpixel binning that is 1/5 of the native pixel size and 3×3 pixel FWHM Gaussian filter smoothing. Green lines represent 33 GHz VLA contours as in Figure 3, white crosses represent the near-IR sources from Scoville et al. (1998) and white diamonds represent the X-ray sources from Clements et al. (2002).

Table 2
Best-fit Parameters for the Extraction Regions Considered in the Main Text

Band	W region			E region			Central 4''5		
	Net counts (error)								
3–8 keV	75 (9)			221 (15)			659 (26)		
6–7 keV	15 (3)			41 (6)			90 (10)		
6–6.4 keV	6 (2)			11 (3)			25 (5)		
6.4–6.7 keV	8 (3)			27 (5)			55 (7)		
Model parameter	Best-fit value								
Spectral model (Power-law + lines)	(a)	(b)	(c)	(a)	(b)	(c)	(a)	(b)	(c)
Γ_{PL}	3.40*	3.40*	3.40*	2.39*	2.39*	2.39*	3.12*	3.12*	3.12*
$F_{\text{PL}} (10^{-4} \text{ cm}^{-2} \text{ s}^{-1} \text{ keV}^{-1})$	$18.30_{-1.72}^{+2.27}$	$18.97_{-1.93}^{+2.07}$	$18.06_{-1.90}^{+2.04}$	$4.48_{-0.67}^{+0.40}$	$5.56_{-0.51}^{+0.55}$	$4.47_{-0.50}^{+0.38}$	$38.65_{-3.42}^{+2.43}$	$44.42_{-2.26}^{+2.37}$	$38.91_{-2.27}^{+2.29}$
$E_{\text{Fe-K}} (\text{keV, rest-frame})$	$6.61_{-0.07}^{+0.06}$	6.4*	6.4*	$6.67_{-0.03}^{+0.03}$	6.4*	6.4*	$6.65_{-0.02}^{+0.02}$	6.4*	6.4*
$F_{\text{Fe-K}} (10^{-7} \text{ cm}^{-2} \text{ s}^{-1})$	$4.01_{-1.59}^{+1.97}$	$2.39_{-1.27}^{+1.59}$	$1.16_{-1.09}^{+1.42}$	$9.43_{-1.91}^{+2.17}$	$1.78_{-1.27}^{+1.51}$	<0.86	$11.92_{-2.07}^{+2.21}$	<5.01	<0.88
$L_{\text{Fe-K}} (10^{40} \text{ erg s}^{-1})$	$0.32_{-0.14}^{+0.13}$	$0.19_{-0.10}^{+0.11}$	$0.09_{-0.07}^{+0.07}$	$0.76_{-0.15}^{+0.17}$	$0.14_{-0.08}^{+0.11}$	<0.04	$0.96_{-0.17}^{+0.17}$	<0.29	<0.06
$\text{EW}_{\text{Fe-K}} (\text{keV})$	$1.22_{-0.53}^{+0.57}$	$0.67_{-0.36}^{+0.43}$	$0.35_{-0.28}^{+0.29}$	$1.76_{-0.43}^{+0.45}$	$0.27_{-0.15}^{+0.23}$	<0.11	$1.02_{-0.19}^{+0.19}$	<0.27	<0.06
$E_{\text{Fe-K}} (\text{keV, rest-frame})$	6.7*	6.7*	6.7*
$F_{\text{Fe-K}} (10^{-7} \text{ cm}^{-2} \text{ s}^{-1})$	$3.33_{-1.58}^{+1.94}$	$9.62_{-1.99}^{+2.16}$	$11.86_{-2.03}^{+2.22}$
$L_{\text{Fe-K}} (10^{40} \text{ erg s}^{-1})$	$0.27_{-0.13}^{+0.15}$	$0.78_{-0.19}^{+0.18}$	$0.96_{-0.08}^{+0.12}$
$\text{EW}_{\text{Fe-K}} (\text{keV})$	$1.04_{-0.47}^{+0.60}$	$1.80_{-0.46}^{+0.48}$	$0.97_{-0.08}^{+0.13}$
C-stat (d.o.f.)	34.9 (29)	47.0 (30)	42.3 (29)	86.3 (66)	137.5 (67)	85.5 (66)	288.1 (211)	352.2 (212)	292.3 (211)
$L_{2-10 \text{ keV}} (10^{40} \text{ erg s}^{-1})$	$1.99_{-0.23}^{+0.20}$	$1.91_{-0.23}^{+0.23}$	$2.01_{-0.23}^{+0.26}$	$3.22_{-0.32}^{+0.31}$	$3.08_{-0.29}^{+0.31}$	$3.23_{-0.33}^{+0.32}$	$6.81_{-0.39}^{+0.39}$	$6.56_{-0.43}^{+0.44}$	$7.13_{-0.30}^{+0.35}$
Model parameter	Best-fit value								
Spectral model (APEC)	(d)			(d)			(d)		
$N_{\text{H}} (10^{22} \text{ cm}^{-2})$	$5.63_{-1.07}^{+3.20}$	$5.65_{-1.32}^{+1.89}$	$5.83_{-0.69}^{+0.90}$	$4.75_{-0.74}^{+0.74}$	$4.75_{-0.74}^{+0.74}$	$2.42_{-0.51}^{+0.79}$	$2.28_{-0.61}^{+1.08}$	$2.28_{-0.61}^{+1.08}$	$2.28_{-0.61}^{+1.08}$
$kT (\text{keV})$	$5.58_{-2.27}^{+5.34}$	$5.44_{-1.51}^{+2.71}$	$5.18_{-1.05}^{+0.79}$	$5.53_{-0.70}^{+1.11}$	$5.53_{-0.70}^{+1.11}$	$5.30_{-1.14}^{+1.26}$	$5.21_{-1.02}^{+1.18}$	$5.21_{-1.02}^{+1.18}$	$5.21_{-1.02}^{+1.18}$
$\text{EM} (10^{-4} \text{ cm}^{-2} \text{ s}^{-1})$	$2.95_{-0.76}^{+1.49}$	$2.89_{-0.72}^{+1.88}$	$4.58_{-0.72}^{+1.29}$	$2.31_{-0.42}^{+0.65}$	$2.31_{-0.42}^{+0.65}$	$7.42_{-0.94}^{+1.22}$	$6.45_{-1.15}^{+1.85}$	$6.45_{-1.15}^{+1.85}$	$6.45_{-1.15}^{+1.85}$
Z	1*	$1.14_{-0.44}^{+0.75}$	1*	$4.14_{-1.29}^{+2.30}$	$4.14_{-1.29}^{+2.30}$	1*	$1.62_{-0.52}^{+0.59}$	$1.62_{-0.52}^{+0.59}$	$1.62_{-0.52}^{+0.59}$
C-stat (d.o.f.)	111.6(40)	111.5(39)	261.6(94)	247.9(93)	247.9(93)	306.8(310)	305.7(309)	305.7(309)	305.7(309)
$L_{0.5-8 \text{ keV}} (10^{40} \text{ erg s}^{-1})$	$3.85_{-0.62}^{+0.70}$	$3.89_{-1.41}^{+1.51}$	$5.89_{-0.89}^{+0.86}$	$5.42_{-1.62}^{+1.52}$	$5.42_{-1.62}^{+1.52}$	$9.59_{-4.46}^{+4.96}$	$9.65_{-3.15}^{+3.55}$	$9.65_{-3.15}^{+3.55}$	$9.65_{-3.15}^{+3.55}$

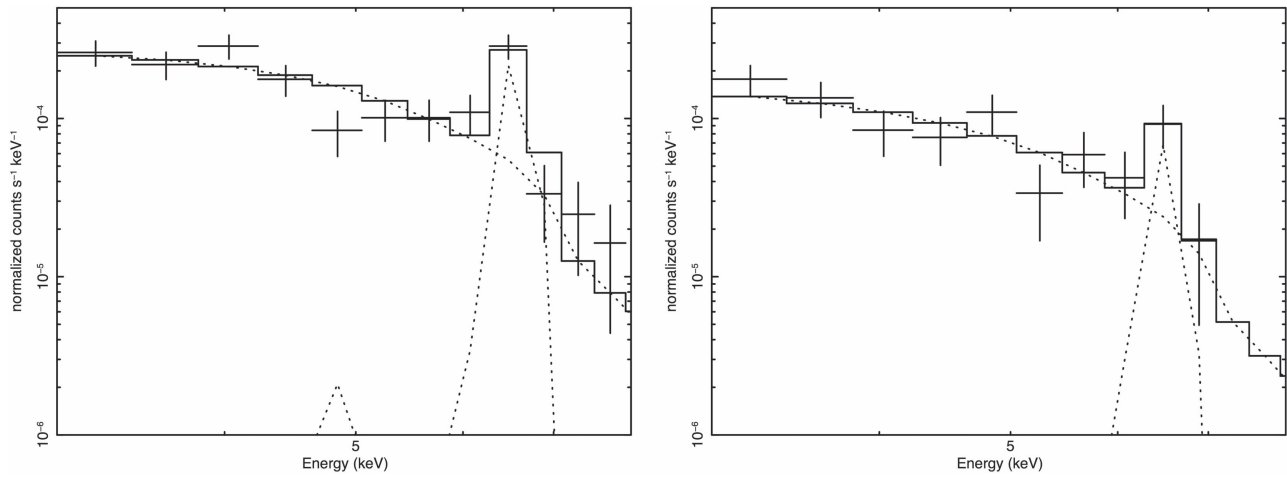


Figure 5. Best fit to the spectra extracted from the regions shown in Figure 2 from the E region (left panel) and the W region (right panel). For clarity only the reflection component and Fe–K line are shown with a dotted line.

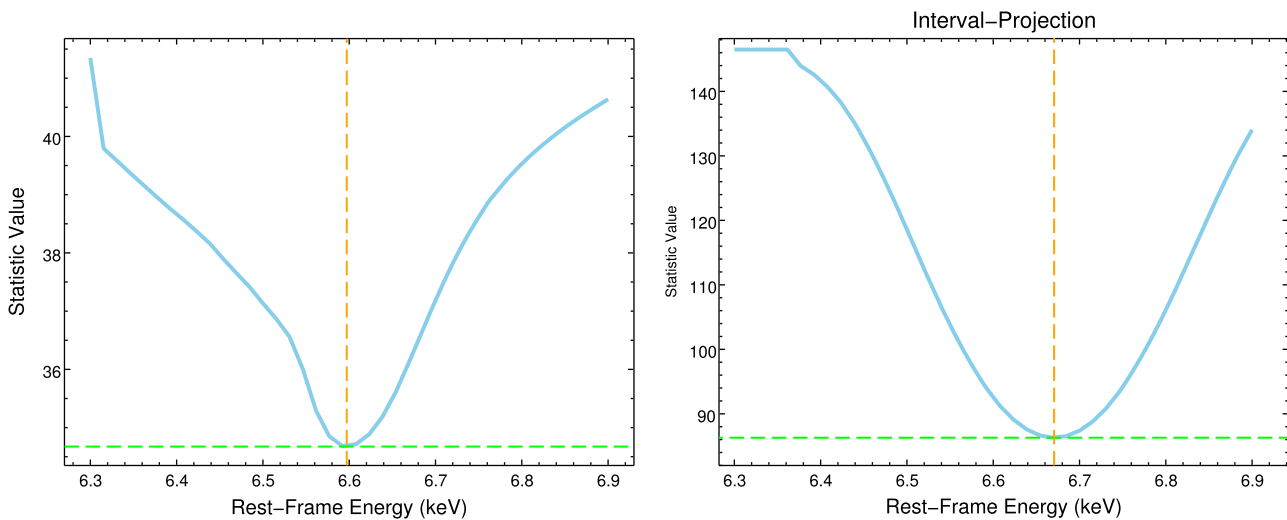


Figure 6. Value of the fit statistic of Model (a) as a function of the rest-frame line energy in the W (left panel) and the E (right panel) nuclei.

2.3. AGN Model

We first used a model typical of CT AGN emission (Levenson et al. 2006), comprising an absorption component fixed to the galactic value $3.9 \times 10^{20} \text{ cm}^{-2}$, a power-law and redshifted Gaussian Fe–K line(s) with width fixed to 100 eV, and possible additional Ar, S, and Ca lines as reported by Iwasawa et al. (2005). We used both XSPEC (ver. 12.8.2¹⁰) and SHERPA¹¹ with identical results. The extracted spectra and the best-fit parameters are presented in Figure 5 and Table 2¹², respectively. Spectra were extracted from the nuclear regions shown in Figure 2 as well as in the entire central region of Arp 220, using a circular region of a $4''5$ radius centered at the coordinates of sources shown in Figure 2.

Due to low statistics, we first fit the power-law component excluding data from 6–7 keV energy range. We then froze the power-law spectral index so obtained and added a redshifted Gaussian Fe–K line with energy free to vary (columns 1, 4, and 7 of Table 2, Model (a)). In order to evaluate the contribution

from neutral and ionized Fe–K separately, we then froze the line rest-frame energy at 6.4 keV (columns 2, 5, and 8 of Table 2, Model (b)) and then added a second line with the rest-frame energy frozen at 6.7 keV (columns 3, 6, and 9 of Table 2, Model (c)) in order to evaluate the relative contribution of the neutral and ionized Fe lines.

In each model, given the contamination of the continuum radiation by the extended emission (suggested by the spatial distributions of continuum photons in Figure 2) and the poor statistics, our estimate of the nuclear continuum luminosity is an upper limit, and the Fe–K EWs must be considered as lower limits.

Model (a): We added a single Gaussian line to the power law. This led to detections of Fe–K line features in both regions, with a comparable EW (1.2 keV and 1.8 keV in the W and the E regions, respectively). As expected from the imaging, the Fe–K line is more luminous in the E nucleus ($0.8 \times 10^{40} \text{ erg s}^{-1}$) with respect to the W nucleus ($0.3 \times 10^{40} \text{ erg s}^{-1}$). As already discussed, the *observed* 2–10 keV luminosities, $3.2 \times 10^{40} \text{ erg s}^{-1}$ (E) and $2.0 \times 10^{40} \text{ erg s}^{-1}$ (W), should be considered as upper limits because of contamination.

¹⁰ <https://heasarc.gsfc.nasa.gov/xanadu/xspec>

¹¹ <http://cxc.harvard.edu/sherpa>

¹² In the following analysis, errors correspond to the 1- σ confidence level for one parameter of interest.

Given the rest-frame line energies (6.67 ± 0.03 and $6.61_{-0.07}^{+0.06}$ keV in the E and the W regions, respectively), Fe XXV appears to be dominant in the Fe–K range, with fluxes of $9.43_{-1.91}^{+2.17} \times 10^{-7} \text{ cm}^{-2} \text{ s}^{-1}$ and $4.01_{-1.59}^{+1.67}$ in the E and the W regions, respectively. In Figure 6 we show the value of the fit statistic as a function of the rest-frame line energy.

We compare our results with those of LaMassa et al. (2011), who extracted a spectrum of the entire central region of Arp 220 using the archival *Chandra*-ACIS observation (observation 00869). Using a circular $4''.5$ radius count extraction region we detected a line at a 6.65 ± 0.02 keV width and an equivalent width of $1.39_{-0.69}^{+1.44}$ keV, compatible with the *XMM-Newton* detection at $6.72_{-0.12}^{+0.10}$ keV (Iwasawa et al. 2005).

Model (b): To assess an upper limit to the neutral Fe–K α contribution, we held the line rest-frame energy fixed at 6.4 keV (Model (b)). Using a circular $4''.5$ radius extraction region like LaMassa et al. (2011), we confirmed their results as only being able to set an upper limit on the Fe–K α EW. We then performed the same spectral fitting in the E and W nuclear regions. As shown in Table 2, due to the lower statistics with respect to the $4''.5$ region, neutral Fe–K α is detected although with a lower significance with respect to Model (a), with line fluxes of $1.78_{-1.27}^{+1.51}$ and $2.39_{-1.27}^{+1.59} \times 10^{-7} \text{ cm}^{-2} \text{ s}^{-1}$ for the E and W nuclei, respectively.

Model (c): We then added a second line with a rest-frame energy fixed at 6.7 keV (Model (c)) to try to evaluate the relative contribution of the Fe–K α and the Fe XXV lines. With this model the neutral Fe line is detected only in the W nucleus region with a flux accounting for $\sim 25\% \pm 10\%$ of the total line flux, while in both the E nucleus and the central $4''.5$ region we can only put an upper limit of $\sim 5 \times 10^{38} \text{ erg s}^{-1}$ on the Fe–K α emission.

To further test the possible contribution of a neutral Fe emission line to the 6–7 keV emission we see in Figure 4, we analyzed the archival *XMM-Newton* observations of Arp 220 discussed in Iwasawa et al. (2005). The data were reduced following a standard procedure, analogous to the one described by Iwasawa et al. (2005). The results are also in agreement: in a continuum plus single-line model we obtain a best-fit peak rest-frame energy of $E = 6.65 \pm 0.04$ keV. However, if we fit the data with two lines with fixed-peak rest-frame energies $E_1 = 6.4$ keV and $E_2 = 6.7$ keV, we obtain the results shown in Figure 7: a neutral component accounting for up to 40% of the observed line flux cannot be ruled out at a 90% confidence level, which is compatible with the fluxes obtained with fixed 6.4 keV lines.

2.4. Thermal Model

Finally, we investigate the possibility for the Fe–K lines to arise from thermal gas emission—possibly from merged supernova (SN) ejecta and stellar winds present during a starburst. To this

end we fitted the 2–8 keV spectra with a collisionally ionized plasma component APEC and an intrinsic absorption component, ZWABS, at the source redshift (Model (d)), with element abundances both fixed at solar values and free to vary, and the results are reported in Table 2. The temperatures of the gas obtained from the fits are ~ 5 keV, with column densities of $\sim 5 \times 10^{22} \text{ cm}^{-2}$ for the W and E regions, and $\sim 2 \times 10^{22} \text{ cm}^{-2}$ in the central $4''.5$ region. The metallicities are found to be $4.58_{-0.72}^{+1.29}$, $1.14_{-0.44}^{+0.75}$, and $1.62_{-0.52}^{+0.59}$ in the E, W, and central $4''.5$ regions, respectively. We notice in particular that the high metallicity obtained in the E nucleus can be due to chemical enrichment by SNe II in a starburst region, producing substantial α -elements but a relatively small amount of Fe. The Fe metallicity in this region is very large—about four times the solar values—but this can be the case for a region with intense star formation (e.g., Fabbiano et al. 2004). We note, however, that this model is disfavored by the large statistics shown in Table 2 indicating that if present, the thermal gas emission is likely to be subdominant with respect to harder emissions, possibly of nuclear origin. The results from Model (d) must be therefore interpreted as upper limits on thermal gas emission.

3. Discussion

Making use of deep *Chandra*-ACIS observation and subpixel binning in narrow spectral bands we have detected three sources of emission in the 6–7 keV band, with the westernmost and easternmost sources coincident with the IR (W) and radio (E) nuclei of Arp 220 (see Figure 4). The spectral analysis (Section 2.2) showed Fe–K lines with large ($\gtrsim 1$ keV) EWs and with the rest-frame line energies of the neutral Fe–K α line larger than 6.4 keV and compatible with the 6.7 keV Fe XXV emission.

3.1. CT AGN Models

In this section we try to constrain the presence of a dual CT AGN in the Arp 220 nuclei. CT AGNs are characterized in the X-rays by a hard high-energy continuum, a “reflection” flat continuum in the ~ 2 –10 keV range, and a high EW ($\gtrsim 1$ keV) 6.4 Fe–K α line (e.g., Matt et al. 1997, 2000). Examples of this merger-driven evolution are given by the pairs of nuclei discovered in the 6.4 keV Fe–K line with *Chandra* in the merger IR luminous galaxy NGC 6240 (Komossa et al. 2003).

As for NGC 6240 (Komossa et al. 2003), Arp 220 is a highly disturbed system of galaxies engaged in a major merging interaction. The physical projected separation of the CT nuclei is ~ 670 pc in NGC 6240 and ~ 380 pc in Arp 220, suggesting that the latter may be in a more advanced stage of merging.

The spectral analysis of the individual W and E nuclei results in the detection of Fe emission lines. The rest-frame energy of the line, however, is larger than the 6.4 keV of the K α line and suggests a contribution from the 6.7 keV shock-ionized Fe XXV line. However, as shown in Figure 7, if we assume that both the 6.4 and the 6.7 keV lines are present in the spectrum, then we obtain an acceptable fit to the *XMM-Newton* data, which allow for a 40% 6.4 keV contribution. The statistics, however, do not allow us to disentangle the 6.4 and 6.7 keV line contribution to the observed emission in the *Chandra* data.

If we then consider that 40% of the Fe–K line flux that we estimate from the *Chandra* spectra is due to the Fe–K α neutral 6.4 keV emission line, then the 2–10 keV emitted luminosities inferred from the Fe–K luminosities are $1.6 \times 10^{42} \text{ erg s}^{-1}$ (E) and $0.5 \times 10^{42} \text{ erg s}^{-1}$ (W). We note that these corrections are

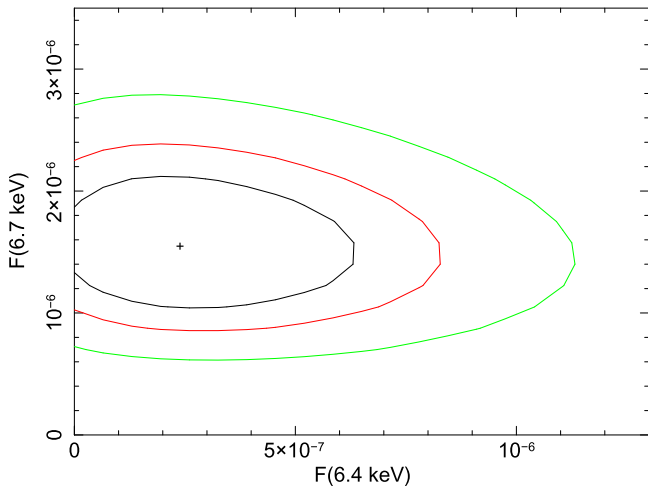


Figure 7. Contour plot for the relative flux of the 6.4 and 6.7 keV lines in a fit where both rest-frame energies are fixed in the *XMM-Newton* data from the nuclear (E+W) region. The contours represent a probability of 68%, 90%, and 99%. Even if a solution with a single 6.7 keV line is the more likely, a contribution of up to 40% by a neutral line is compatible with the data at a 90% confidence level.

calibrated on “standard” obscured Seyfert galaxies, with an X-ray reflection efficiency of a few percent (Levenson et al. 2006). Hard X-ray observations of ULIRGs have demonstrated that on average this efficiency is much lower for these sources (Teng et al. 2009; Nardini & Risaliti 2011). Consequently, the intrinsic X-ray luminosity of the two AGN detected here could be significantly higher. Considering the values for a standard reflection efficiency, the inferred X-ray luminosity is at least a factor of three higher than that expected from a pure starburst with the bolometric luminosity of Arp 220 (Ranalli et al. 2003).

The two nuclei have radio fluxes of 92.4 (E) and 114.6 (W) mJy at 33 GHz (Barcos-Muñoz et al. 2015), and X-ray-to-optical slopes of $\alpha(ox) \approx 2.75$. From the inferred 2–10 keV emitted luminosities of the two nuclear sources we evaluate bolometric luminosities assuming typical AGN SEDs (Elvis et al. 1994, 2002) and the X-ray reflection efficiency of Seyfert galaxies. The estimated AGN bolometric luminosities, which should be regarded as lower limits, are $\sim 8.3 \times 10^{43}$ erg s $^{-1}$ (E) and $\sim 2.5 \times 10^{43}$ erg s $^{-1}$ (W). These represent only $\sim 1\%$ of the Arp 220 bolometric luminosity $\sim 6 \times 10^{45}$ erg s $^{-1}$ (Sanders et al. 1988), confirming that overall the emission of Arp 220 is dominated by the starburst component. We note that the AGN luminosity evaluated with IR data by Veilleux et al. (2009) and Nardini et al. (2010) is much higher than that inferred from our X-ray analysis, which is suggestive of heavy or nearly total obscuration. Lower limits on associated black hole masses can be evaluated assuming an Eddington limited accretion (with a standard 10% accretion rate to the luminosity conversion efficiency), yielding $M \sim 5 \times 10^5 M_{\odot}$ (E) and $\sim 1 \times 10^5 M_{\odot}$ (W).

The lack of 6.4 keV emission may result from a limited visibility of the inner torus surrounding the nuclear AGNs, allowing only the emission of ionized gas to be visible (Iwasawa et al. 2005). To test this possibility we produced a hardness ratio (HR) map of the central region of this source (Figure 8, right panel). This map has been obtained from the event maps in the soft (S) 0.3–2 keV and hard (H) 2–8 keV bands with a subpixel binning that is 1/4 of the native pixel size, evaluating $HR = (H - S)/(H + S)$ and then applying a

3×3 pixel FWHM Gaussian filter smoothing. The white contours in the figure indicate levels of HR from 0.1 to 0.8, in increments of 0.1. We then binned the event maps using these contours, producing the HR binned map presented in the central panel of Figure 8. In this panel we superimpose in yellow the 33 GHz VLA contours from Barcos-Muñoz et al. (2015) to highlight the “bridge” of HR ~ 0.8 that connects the two nuclei detected in both radio and X-ray (see Figure 3) and corresponding with the X4 source reported by Clements et al. (2002). On the right panel of Figure 8 we present a significance map of the HR binned map, evaluated as the ratio between the uncertainty on the HR and the HR itself, showing that this “bridge” feature is significant at an 8σ level. We then produced simulated spectra, assuming a power-law spectrum with a slope of 1.8 (as appropriate for AGN emission) and, in addition to the galactic absorption, an intrinsic absorption component at the source redshift, and we then evaluated the observed HR that such spectra would yield. In this way we converted the binned HR map to the intrinsic absorption column map presented in the left panel of Figure 9, where the logarithmic values of $N_{\text{H}}/\text{cm}^{-2}$ are presented, with the 33 GHz VLA contours overplotted in blue. On the right panel of Figure 9 we show the map of the corresponding error on $\log(N_{\text{H}}/\text{cm}^{-2})$ evaluated from the uncertainty on the HR. We see that in the region connecting the two nuclei we reach $N_{\text{H}} \sim 10^{22.5}$ cm $^{-2}$, similar to that obtained from the spectral fitting with Model (d) but about four orders of magnitude lower than the value of $N_{\text{H}_2} = 2.6 \times 10^{26}$ cm $^{-2}$ reported by Scoville et al. (2017) for the W nucleus, indicating again that the AGN contribution to X-ray emission represents a subdominant component with respect to star formation activity (see next section).

3.2. Star Formation Activity

The nuclear region of Arp 220 is the site of an intense star formation with $\text{SFR} \sim 340 M_{\odot} \text{ yr}^{-1}$ (Baan 2007; Barcos-Muñoz et al. 2015). The X-ray expected luminosity from X-ray binaries, evaluated using the correlation between the galaxy 2–10 keV luminosity and the SFR provided by the *Chandra* survey of luminous IR galaxies (LIRGs) (Lehmer et al. 2010), exceeds the observed luminosity by one order of magnitude. However, it is possible, as suggested by the previous discussion, that X-ray binaries in Arp 220 are located in compact star-forming regions buried under thick absorption columns with $N_{\text{H}} \gg 10^{23}$ cm $^{-2}$ that dims the emission in the 2–10 keV band (Lehmer et al. 2010).

As discussed before, the Fe XXV emission may be related with the thermal gas from merged SN ejecta and stellar winds present during a starburst, as exemplified by the extended Fe XXV regions of the merger-dual CT AGN NGC 6240 (Wang et al. 2014). An extended Fe XXV line emission is also observed in other well-known starburst galaxies like NGC 253 and M82 (e.g., Pietsch et al. 2001; Mitsuishi et al. 2011), the merger-dual CT AGN NGC 6240 (Wang et al. 2014), and the integrated spectrum of a number of LIRG/ULIRG systems (Iwasawa et al. 2009), suggesting the existence of similar high-temperature plasma.

According to the starburst-driven superwind model, a hot gas bubble of internally shocked wind material with a temperature of several keV forms in the region of intense star formation (Chevalier & Clegg 1985; Suchkov et al. 1994; Strickland & Heckman 2007); this hot gas eventually flows outward as a high-speed (a few 1000 km s $^{-1}$) wind. As a comparison, we note that

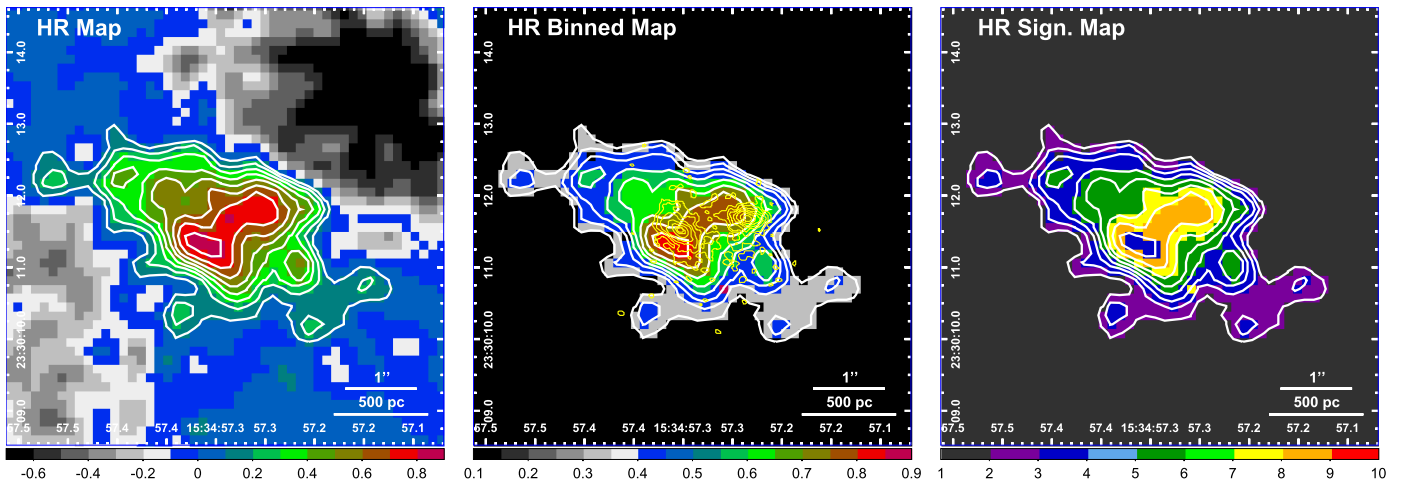


Figure 8. Left panel: HR map for the central region of Arp 220 with a subpixel binning that is $1/4$ of the native pixel size and a 3×3 pixel FWHM Gaussian filter smoothing. The white contours indicate levels of HR from 0.1 to 0.8, in increments of 0.1. Central panel: same as left panel, but with the map binned using the contour levels. In yellow we show the 33 GHz VLA contours. Right panel: significance map of the HR binned map.

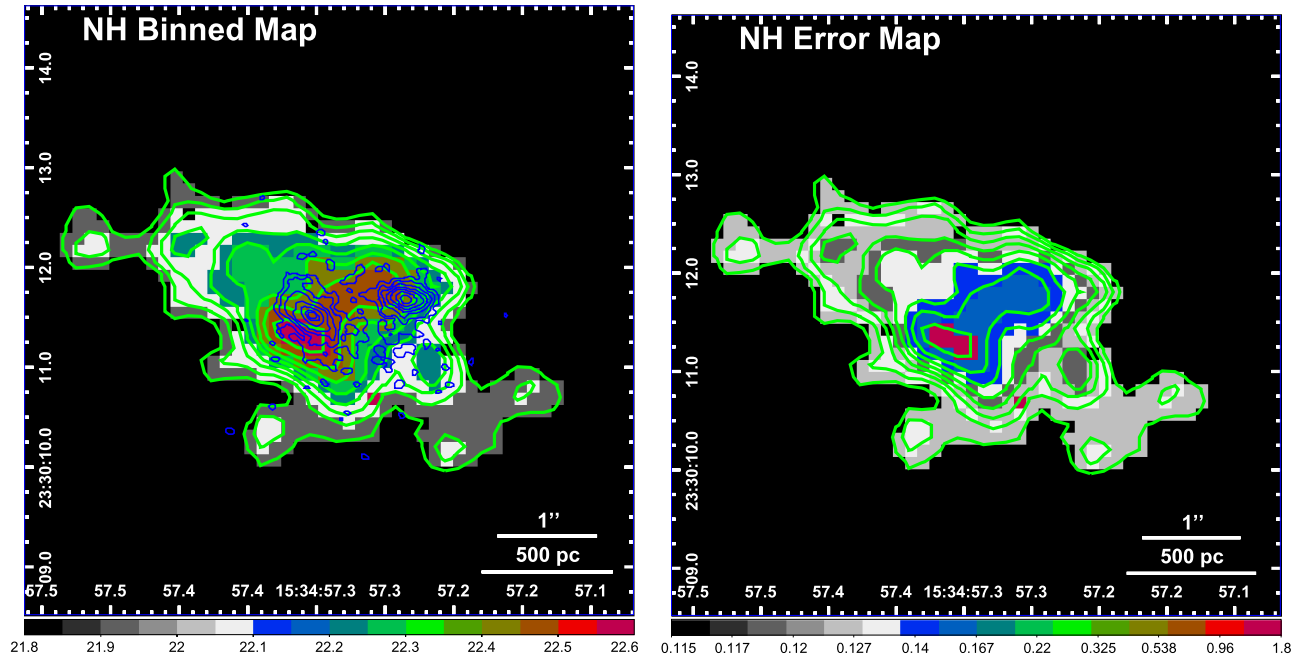


Figure 9. Left panel: logarithmic map of the absorption column as evaluated from the HR map presented in the central panel of Figure 8 assuming a power-law spectrum with a 1.8 slope. The 33 GHz VLA contours are overplotted in blue. Right panel: map of the error on $\log(N_{\text{H}}/\text{cm}^2)$ evaluated from the uncertainty on the HR.

the observed diffuse hard X-ray emission in Arp 220 has a luminosity one order of magnitude higher than that observed in the classic superwind system M82 ($L_{2-10 \text{ keV}} = 4 \times 10^{39} \text{ erg s}^{-1}$; Strickland & Heckman 2007). Following the calculation of Wang et al. (2014) we can evaluate the shock velocity $v = \sqrt{16 kT/3\mu}$ (where μ is the mean mass per particle and k is Boltzmann's constant) from the observed gas temperature $\sim 5 \text{ keV}$, obtaining $v \simeq 2000 \text{ km s}^{-1}$. Such velocities are unlikely to be due to shocks induced by the merging process of galaxies that collide with velocities of the order of hundreds of km s^{-1} even in the case of direct-collision systems (Braine et al. 2003), and they are also larger than the velocity estimated from the CO line width of $500\text{--}600 \text{ km s}^{-1}$ (Sakamoto et al. 2008; Scoville et al. 2017).

To further investigate whether the thermal energy content of the hot gas could be powered by the thermalization of SNe shocks, we compare the thermal gas energy with the kinetic energy input from the SNe during the starburst. Using the Fe XXV line emission as a tracer for the extent of the hottest thermal component and following the method of Richings et al. (2010), we obtain—assuming a filling factor of 1%—the hot gas masses of $2.6 \times 10^5 M_{\odot}$ and $6.6 \times 10^5 M_{\odot}$ for the W and the E nuclei, respectively, from the emission measure. For solar abundances this yields an Fe mass of $6.4 \times 10^2 M_{\odot}$ and $1.7 \times 10^3 M_{\odot}$ for the W and the E nuclei, respectively. From the temperatures we get from the spectral fit we obtain a thermal energy of $E_{\text{th,W}} = 1.3 \times 10^{55} \text{ erg}$ and $E_{\text{th,E}} = 3.1 \times 10^{55} \text{ erg}$ for the W and the E nuclei, respectively. Assuming an SN rate

for Arp 220 of 4 yr^{-1} (Lonsdale et al. 2006) and that 10% of the kinetic energy input (10^{51} erg per SN) is converted into thermal energy of the hot gas (Chevalier & Clegg 1985; Thornton et al. 1998), we obtain that the total energy deposited during the past starburst is $\sim 4 \times 10^{50}$ erg yr^{-1} . Anantharamaiah et al. (2000) proposed for Arp 220 a star formation model consisting of multiple starbursts of a very high SFR ($\sim 10^3 M_{\odot} \text{ yr}^{-1}$) and a short duration ($\sim 10^5$ year). With this starburst period we obtain that the gas thermal energy is comparable with the kinetic energy input from the SNe. On the other hand, the cooling time of this thermal gas is $t_{\text{cool}} = E_{\text{th}}/L_X \sim 50$ Myr, which is far larger than the starburst duration, allowing the X-ray bright phases to survive once the starburst ceases. Note that such a short starburst can also explain the lack of X-ray point sources, that with an SFR of ($\sim 10^3 M_{\odot} \text{ yr}^{-1}$) would attain a luminosity of $\sim 10^{42}$ erg s^{-1} (Mineo et al. 2012). We can also compare the Fe yield SNe over the starburst with the Fe mass evaluated from the spectral fitting of the thermal gas emission. Using an ejected Fe mass per SN II of $8.4 \times 10^{-2} M_{\odot}$ (Iwamoto et al. 1999), an SN of 4 yr^{-1} (Lonsdale et al. 2006) over a starburst of 10^5 year would yield $\sim 3.4 \times 10^4 M_{\odot}$ of Fe, more than enough to account for the Fe mass of $1.7 \times 10^3 M_{\odot}$ and $6.4 \times 10^2 M_{\odot}$ evaluated before for the E and the W nuclei, respectively. However, a continuous SFR of $350 M_{\odot} \text{ yr}^{-1}$ over a period of $\sim 1.5 \times 10^7$ year (Anantharamaiah et al. 2000) would yield an SNe kinetic energy input exceeding the gas thermal energy by two orders of magnitude and a cooling time of about three times the starburst duration, with a yield of $\sim 3.4 \times 10^6 M_{\odot}$ of Fe.

These estimates demonstrate that the observed diffuse thermal gas traced by the highly ionized Fe line emission in Arp 220 is consistent with being heated by SNe shocks in the starburst, although high-velocity winds from hidden AGNs may also be present.

4. Conclusions

We presented an imaging and spectral analysis of the nuclear region of the ULIRG merger Arp 220 that makes use of deep *Chandra*-ACIS observations that sum to ~ 300 ks. Narrowband spectral imaging with a subpixel resolution of the innermost nuclear region reveals two Fe–K emitting sources, spatially coincident with the IR and radio-emitting nuclear clusters and separated by $1''$ (~ 380 pc at a distance of ~ 80 Mpc). We estimate an Fe–K equivalent width of ~ 1 keV or possibly greater for both sources and observed 2–10 keV luminosities of $L_X \sim 2 \times 10^{40}$ erg s^{-1} (W) and $\sim 3 \times 10^{40}$ erg s^{-1} (E).

In the narrow 6–7 keV band the emission from these regions is dominated by the 6.7 keV Fe XXV emission line, suggesting a contribution from collisionally ionized gas or starburst regions (see also Iwasawa et al. 2005). The nuclear regions appear to be filled with a thermal gas at ~ 5 keV whose energetic content can be accounted for by a kinetic energy injection in the interstellar medium by SNe II. As NGC 6240 (Wang et al. 2014), the thermal gas surrounding the nuclei and responsible for the hard X-ray emission has a thermal energy comparable with the kinetic energy injected in the surrounding medium by SNe II in a short ($\sim 10^5$ year) starburst episode.

The X-ray emission from the E nucleus appears morphologically coincident with the disk emission as mapped by 2.6 mm continuum ALMA and CO 2-1 IRAM PdBI data, suggesting starburst dominance in this region. However, *Chandra* data allow us to constrain the contribution from (possibly dust-obscured) AGNs. In fact, our analysis of the *XMM-Newton* data

confirms the presence of the Fe XXV emission line but allows 40% of the narrowband emitted flux from the neutral 6.4 keV line. Based on the Fe–K detections, we infer lower limits on the bolometric luminosity of the AGNs in Arp 220 of 8.3×10^{43} erg s^{-1} for the E nucleus and $\sim 2.5 \times 10^{43}$ erg s^{-1} for the W nucleus. These are a few percent of the total ULIRG bolometric luminosity, confirming that overall the emission of this source is dominated by the starburst component as estimated from the mid-IR spectroscopy (Veilleux et al. 2009; Nardini et al. 2010). Our results are consistent with previous multi-wavelength indications of nuclear activity in Arp 220 (see Section 1) and they strengthen the evolutionary association of merging and nuclear activity in galaxies (e.g., Hopkins et al. 2008; Van Wassenhove et al. 2012).

These results have only been possible because of the unmatched *Chandra*-ACIS spatial resolution coupled with the use of subpixel imaging in narrow spectral bands, which allow us to perform narrowband, high-resolution imaging that gives us a clear picture of the nuclear surroundings.

We acknowledge useful comments and suggestions by our anonymous referee. This work is supported by NASA grant G04-15107X (P. I. Fabbiano). JW acknowledges support from the National Key Program for Science and Technology Research and Development 2016YFA0400702 and the NSFC grants 11473021, 11522323. We acknowledge support from the CXC, which is operated by the Smithsonian Astrophysical Observatory for and on behalf of NASA under contract NAS8-03060. This research has made use of data obtained from the *Chandra* Data Archive and software provided by the CXC in the application packages CIAO and Sherpa. This research has made use of Iris software provided by the U.S. Virtual Astronomical Observatory, which is sponsored by the National Science Foundation and NASA.

References

- Aalto, S., Wilner, D., Spaans, M., et al. 2009, *A&A*, 493, 481
 Anantharamaiah, K. R., Viallefond, F., Mohan, N. R., Goss, W. M., & Zhao, J. H. 2000, *ApJ*, 537, 613
 Baan, W. A. 2007, in IAU Symp. 242, *Astrophysical Masers and their Environments*, ed. J. M. Chapman & W. A. Baan (Cambridge: Cambridge Univ. Press), 437
 Baan, W. A., & Haschick, A. D. 1995, *ApJ*, 454, 745
 Barcos-Muñoz, L., Leroy, A. K., Evans, A. S., et al. 2015, *ApJ*, 799, 10
 Braine, J., Davoust, E., Zhu, M., et al. 2003, *A&A*, 408, L13
 Carter, C., Karovska, M., Jerius, D., Glotfelty, K., & Beikman, S. 2003, *adass XII*, 295, 477
 Chevalier, R. A., & Clegg, A. W. 1985, *Natur*, 317, 44
 Clements, D. L., McDowell, J. C., Shaked, S., et al. 2002, *ApJ*, 581, 974
 Contini, M. 2013, *MNRAS*, 429, 242
 Davis, J. E. 2001, *ApJ*, 562, 575
 Di Matteo, T., Springel, V., & Hernquist, L. 2005, *Natur*, 433, 604
 Downes, D., & Eckart, A. 2007, *A&A*, 468, L57
 Elvis, M., Risaliti, G., & Zamorani, G. 2002, *ApJL*, 565, L75
 Elvis, M., Wilkes, B. J., McDowell, J. C., et al. 1994, *ApJS*, 95, 1
 Esch, D. N., Connors, A., Karovska, M., & van Dyk, D. A. 2004, *ApJ*, 610, 1213
 Fabbiano, G., Baldi, A., King, A. R., et al. 2004, *ApJL*, 605, L21
 Fruscione, A., McDowell, J. C., Allen, G. E., et al. 2006, *Proc. SPIE*, 6270, 62701V
 Governato, F., Colpi, M., & Maraschi, L. 1994, *MNRAS*, 271, 371
 Harris, D. E., Mossman, A. E., & Walker, R. C. 2004, *ApJ*, 615, 161
 Hopkins, A. M., McClure-Griffiths, N. M., & Gaensler, B. M. 2008, *ApJL*, 682, L13
 Iwamoto, K., Brachwitz, F., Nomoto, K., et al. 1999, *ApJS*, 125, 439
 Iwasawa, K., Sanders, D. B., Evans, A. S., et al. 2005, *MNRAS*, 357, 565
 Iwasawa, K., Sanders, D. B., Evans, A. S., et al. 2009, *ApJL*, 695, L103

- Karovska, M., Carilli, C. L., Raymond, J. C., & Mattei, J. A. 2007, *ApJ*, **661**, 1048
- Karovska, M., Schlegel, E., Hack, W., Raymond, J. C., & Wood, B. E. 2005, *ApJL*, **623**, L137
- Kim, D.-C., & Sanders, D. B. 1998, *ApJS*, **119**, 41
- Komossa, S., Burwitz, V., Hasinger, G., et al. 2003, *ApJL*, **582**, L15
- König, S., García-Marín, M., Eckart, A., Downes, D., & Scharwächter, J. 2012, *ApJ*, **754**, 58
- LaMassa, S. M., Heckman, T. M., Ptak, A., et al. 2011, *ApJ*, **729**, 52
- Lehmer, B. D., Alexander, D. M., Bauer, F. E., et al. 2010, *ApJ*, **724**, 559
- Levenson, N. A., Heckman, T. M., Krolik, J. H., Weaver, K. A., & Życki, P. T. 2006, *ApJ*, **648**, 111
- Li, J., Kastner, J. H., Prigozhin, G. Y., & Schulz, N. S. 2003, *ApJ*, **590**, 586
- Lonsdale, C. J., Diamond, P. J., Thrall, H., Smith, H. E., & Lonsdale, C. J. 2006, *ApJ*, **647**, 185
- Magorrian, J., Tremaine, S., Richstone, D., et al. 1998, *AJ*, **115**, 2285
- Matt, G., Fabian, A. C., Guainazzi, M., et al. 2000, *MNRAS*, **318**, 173
- Matt, G., Guainazzi, M., Frontera, F., et al. 1997, *A&A*, **325**, L13
- Mayer, L., Kazantzidis, S., Madau, P., et al. 2007, *Sci*, **316**, 1874
- Mineo, S., Gilfanov, M., & Sunyaev, R. 2012, *MNRAS*, **419**, 2095
- Mitsuishi, I., Yamasaki, N. Y., & Takei, Y. 2011, *ApJL*, **742**, L31
- Nardini, E., & Risaliti, G. 2011, *MNRAS*, **415**, 619
- Nardini, E., Risaliti, G., Watabe, Y., Salvati, M., & Sani, E. 2010, *MNRAS*, **405**, 2505
- Paggi, A., Wang, J., Fabbiano, G., Elvis, M., & Karovska, M. 2012, *ApJ*, **756**, 39
- Perlman, E. S., Padgett, C. A., Georganopoulos, M., et al. 2010, *ApJ*, **708**, 171
- Pietsch, W., Roberts, T. P., Sako, M., et al. 2001, *A&A*, **365**, L174
- Planck Collaboration, Ade, P. A. R., Aghanim, N., et al. 2016, *A&A*, **594**, A13
- Ranalli, P., Comastri, A., & Setti, G. 2003, *A&A*, **399**, 39
- Rangwala, N., Maloney, P. R., Glenn, J., et al. 2011, *ApJ*, **743**, 94
- Richings, A. J., Fabbiano, G., Wang, J., & Roberts, T. P. 2010, *ApJ*, **723**, 1375
- Risaliti, G., Maiolino, R., & Salvati, M. 1999, *ApJ*, **522**, 157
- Rots, A. H., & Budavári, T. 2011, *ApJS*, **192**, 8
- Sakamoto, K., Wang, J., Wiedner, M. C., et al. 2008, *ApJ*, **684**, 957
- Sanders, D. B., & Mirabel, I. F. 1996, *ARA&A*, **34**, 749
- Sanders, D. B., Soifer, B. T., Elias, J. H., et al. 1988, *ApJ*, **325**, 74
- Scoville, N., Murchikova, L., Walter, F., et al. 2017, *ApJ*, **836**, 66
- Scoville, N., Sheth, K., Walter, F., et al. 2015, *ApJ*, **800**, 70
- Scoville, N. Z., Evans, A. S., Dinshaw, N., et al. 1998, *ApJL*, **492**, L107
- Siemiginowska, A., Stawarz, Ł., Cheung, C. C., et al. 2007, *ApJ*, **657**, 145
- Soifer, B. T., Sanders, D. B., Madore, B. F., et al. 1987, *ApJ*, **320**, 238
- Strickland, D. K., & Heckman, T. M. 2007, *ApJ*, **658**, 258
- Suchkov, A. A., Balsara, D. S., Heckman, T. M., & Leitherer, C. 1994, *ApJ*, **430**, 511
- Teng, S. H., Veilleux, S., Anabuki, N., et al. 2009, *ApJ*, **691**, 261
- Thornton, K., Gaudlitz, M., Janka, H.-T., & Steinmetz, M. 1998, *ApJ*, **500**, 95
- Tunnard, R., Greve, T. R., Garcia-Burillo, S., et al. 2015, *ApJ*, **800**, 25
- Van Wassenhove, S., Volonteri, M., Mayer, L., et al. 2012, *ApJL*, **748**, L7
- Varenus, E., Conway, J. E., Martí-Vidal, I., et al. 2016, *A&A*, **593**, A86
- Veilleux, S., Rupke, D. S. N., Kim, D.-C., et al. 2009, *ApJS*, **182**, 628
- Wang, J., Fabbiano, G., Elvis, M., et al. 2011a, *ApJ*, **736**, 62
- Wang, J., Fabbiano, G., Elvis, M., et al. 2011b, *ApJ*, **742**, 23
- Wang, J., Fabbiano, G., Risaliti, G., et al. 2011c, *ApJ*, **729**, 75
- Wang, J., Nardini, E., Fabbiano, G., et al. 2014, *ApJ*, **781**, 55